Full Length Article

Hard X-ray emission spectroscopy in liquids using MHz XFEL source and JUNGFRAU detectors

M. Biednov [a],*, H. Yousef [a], F. Otte [a,b], T.-K. Choi [a,1], Y. Jiang [a], P. Frankenberger [a], M. Knoll [a], P. Zalden [a], M. Ramilli [a], W. Gawelda [c,d,e], S.E. Canton [a], F. Alves Lima [a], C. Milne [a,*], D. Khakhulin [a,*]

[a] European XFEL, Holzkoppel 4, 22869 Schenefeld, Germany
[b] Fakultät für Physik, Technical University Dortmund, Otto-Hahn-Str. 4, 44227 Dortmund, Germany
[c] Departamento de Química, Universidad Autónoma de Madrid, 28049 Madrid, Spain
[d] IMDEA-Nanociencia, Calle Faraday 9, 28049 Madrid, Spain
[e] Faculty of Physics, Adam Mickiewicz University, 61-614 Poznan, Poland

ABSTRACT

X-ray free-electron lasers (XFEL) provide unique opportunities for hard X-ray emission spectroscopy (XES) in solution phase by enabling femtosecond temporal resolution. The high brilliance and MHz repetition rate of such sources drive the development of specialized sample delivery systems to overcome the challenges of sample degradation, as well as major advances of multiple-gain detectors to fully utilize the high dynamic range required for X-ray detection. This paper addresses the experimental limitations that arise in a typical XES experiment performed on fast liquid jets at the MHz repetition rate of the European XFEL. Using a low-noise gain-switching JUNGFRAU detector allows taking advantage of the high dynamic range and high sensitivity, but restricts a single-shot detection due to the limited frame rate. The gain transition regions of the detector response may exhibit nonlinear behavior that can be identified and efficiently corrected using the internal reference-based normalization and linearization approaches described here.

1. Introduction

Hard X-ray emission spectroscopy (XES) is a powerful element-specific technique for investigating the local electronic state of the absorbing atom and its vicinity [1–3]. XES has been successfully applied to various transition-metal-based molecular compounds both in solid state and in solution phase [4–9] and in particular to Fe^{II}-based spin-crossover (SCO) complexes [10]. In such systems, the specific sensitivity of XES to the local spin combined with the high temporal resolution of a pump-probe experiment allows directly observing and tracking the evolution of charge and spin states after photo-excitation [11–14]. The resulting understanding of the complex interplay between the electronic state of central metal ion and its ligand environment in the course of photochemical processes has provided a firm foundation towards engineering molecular complexes with desired functionalities [15–17]. This concept has expanded beyond the families of prototypical mononuclear complexes and is now successfully applied to a wide variety of biologically-relevant and application-specific molecular systems [18–21].

The advent of hard X-ray free-electron lasers (FEL) has enabled femtosecond temporal resolution for pump-probe XES experiments while significantly reducing the data acquisition time owing to greatly increased peak brightness of the radiation. The development was further boosted by the implementation of superconducting accelerating cavities for FELs, allowing to increase the average number of femtosecond X-ray pulses per second by more than two orders of magnitude compared to the non-superconducting FELs [22]. For example, the European XFEL (EuXFEL) source was designed to deliver 27 000 X-ray pulses per second which arrive in "bursts", the so-called pulse-trains. In regular operation the EuXFEL delivers 10 trains per second, each containing up to 2700 pulses with an intra-train repetition rate of up to 4.5 MHz. The high total X-ray flux available for femtosecond pump-probe experiments offers proportionally reduced data acquisition time, while delivering high quality data even for dilute solutions and intrinsically very weak signals from low probability transitions like the structurally sensitive valence-to-core XES [23–25]. Although the high peak flux and MHz repetition rate are the enabling factors for many experimental techniques, they often pose technical challenges e.g., required fast sample exchange,

* Corresponding authors.
E-mail addresses: mykola.biednov@xfel.eu (M. Biednov), christopher.milne@xfel.eu (C. Milne), dmitry.khakhulin@xfel.eu (D. Khakhulin).
[1] Present address: XFEL division, Pohang Accelerator Laboratory, Jigok-ro 127-80, 37673 Pohang, Republic of Korea.
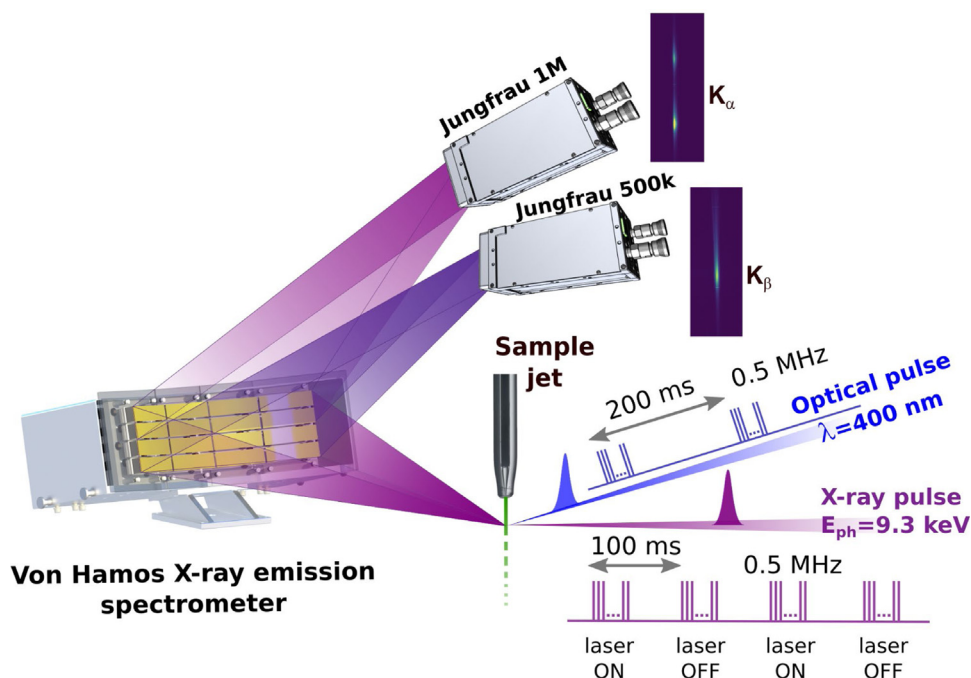
Fig. 1. Experimental setup for pump-probe XES experiments in solutions at the FXE instrument.

high dynamic range of detection, high collection rates, as well as high throughput of data acquisition and processing in general.

At the instrument for Femtosecond X-ray Experiments (FXE) [26,27] of EuXFEL facility transient X-ray emission spectra are typically measured using a 16-crystal energy-dispersive von Hamos-type spectrometer [28–30] and an area detector. For a given cylindrical crystal analyzer the spectrometer covers a broad energy range in a single shot thus allowing to record the entire emission lines of characteristic spectra without scanning, or when combining various analyzers in the spectrometer even collect multiple emission lines from one or several chemical elements [27,31]. Two viable data acquisition methods are to use either a MHz frame rate detector to record spectra shot-to-shot, or a more conventional low frame rate detector collecting train-integrated spectra, i.e. at 10 Hz for EuXFEL. Most available MHz rate 2D detectors have inherently relatively high read noise of fast electronics and typically larger pixels due to on-chip memory cells. At the same time it has been shown that beam pointing and pulse arrival time stability within a pulse train of EuXFEL are significantly higher than those observed from train-to-train [32,33] or at lower sub-kHz repetition rates. This is related to the fact that most mechanical vibrations and sources of drifts appear static at MHz repletion rates, not contributing to the intra-train noise and jitter, while the burst-mode operation enables additional feedback and diagnostics mechanisms [22]. As a result, the integration of all pulses within a train does not become a limiting factor for temporal resolution or pointing stability in the majority of non-resonant pump-probe XES experiments at FXE, provided that inter-train corrections are applied based on the respective diagnostics data.

At the FXE instrument time-resolved XES signals are routinely detected using the gain-switching JUNGFRAU (JF) detector developed at the Paul Scherrer Institute [34,35] that is operated at 10 Hz frame rate, thus collecting train-integrated images of X-ray emission spectra. The JF is a hybrid charge-integrating pixel detector, which simultaneously offers low noise and high dynamic range for hard X-ray detection. This is achieved by employing three preamplifier stages with different gain factors for each pixel. The preamplifier circuit dynamically selects one of the three gain stages from high (G0), medium (G1) or low (G2), depending on the amount of accumulated charge in a given pixel. The JF has high signal-to-noise ratio (SNR) and single photon sensitivity at the high gain stage (G0) for photons with energy above

approximately 2 keV. The saturation level is 10^4 photons of 12 keV energy for the signal at the low gain stage (G2). This makes the JF a suitable choice for applications requiring simultaneous detection of the relatively weak and the strong hard X-ray emission lines over a wide dynamic range. However, similarly to other adaptive gain detectors, the raw signal may exhibit nonlinearity especially around the gain transition regions [36,37] and therefore the detection response requires detailed characterization and calibration. Moreover, since intense X-ray pulses from XFEL focused to a micron-size spot may destroy condensed phase samples, a special approach is required to verify their integrity or the sufficient exchange rate from shot-to-shot even though the detector is not capable of MHz pulse-resolved data collection. In this work, we present a universal self-referenced approach for characterization and corrections of spectral image data collected in femtosecond XES measurements performed at MHz pulse rates using a low frame rate JF detector.

2. Experimental setup

Validation of the detection method was performed in a pump-probe X-ray emission measurement at the FXE instrument of the European XFEL facility using the standard setup for liquid chemistry experiments [27,38]. The setup and the acquisition approach are schematically shown in Fig. 1.

An aqueous solution of $[Co(terpy)_2]^{2+}$ (terpy = 2,2';6',2"-terpyridine) at 10 mM concentration was delivered to the interaction region by means of a liquid jet system. The sample solution was flown in a closed-loop by a HPLC pump (Shimadzu LC-20AP) through a round glass nozzle with 100 μm diameter (Advanced Microfluidic Systems GmbH - AdMiSys). For collection of XES data the jet speed was set to the maximum of approximately 60 m/s, ensuring sample replenishment at 564 kHz intra-train repetition rate of the X-ray pulses. The interaction region as well as the surrounding enclosing the interaction region, the von Hamos spectrometer and JF detectors was filled with helium gas, using a specially designed chamber with 25 μm thick Kapton windows. The optical absorption spectrum of the studied solution was continuously monitored with an inline UV–Vis spectrometer, to ensure that no sample degradation nor concentration change occurred during the measurements.

The incoming X-ray photon energy was set to 9.3 keV and had a SASE-limited spectral bandwidth ($\Delta E/E \sim 0.2\%$, "pink beam"). The X-ray beam was focused with beryllium compound refractive lenses to a round spot of approximately 7 μm diameter at FWHM. Each X-ray pulse train contained up to 150 pulses with average pulse energy at the sample of approximately 350 μJ. X-ray emission from the sample was collected using the 16-crystal dispersive von Hamos-type emission spectrometer from FXE, equipped with two sets of cylindrically bent analyzer crystals with 0.5 m radius of curvature for simultaneous detection of Kα and Kβ emission lines of cobalt. Si(531) analyzers were used for Co Kα line and Ge(111) for Co Kβ emission with corresponding Bragg angles of 77 and 82.9 degrees. Spectra from individual crystals were focused and overlapped on the detector to improve SNR and signal-to-background ratio. Due to a relatively large difference in the analyzer Bragg angles for the Co Kα and Kβ emission lines, two JF detectors were used: JF 1M for collection of K$\alpha_{1,2}$ emission and an additional JF 500 K for collection of the K$\beta_{1,3}$ emission spectra.

The liquid jet sample was excited by 400 nm radiation, 70 fs FWHM pulse duration, generated as the second harmonic of the main beam from the pump-probe laser system (PPL), developed at EuXFEL [39]. The excitation pulse energy at the sample was varied between 16 and 34 μJ. The focus size of the optical laser beam was set to ca. 73×62 μm^2 FWHM and the crossing angle between the pump laser beam and the X-rays was approx. 12 degrees. The pump laser was synchronized to the XFEL by an all-optical synchronization scheme, resulting in an expected relative X-ray/optical pulse arrival time jitter on the order of 60 fs FWHM [32] and overall width of the instrument response function at FXE of approximately 115 fs FWHM [27] . The intra-train repetition rate and the number of pulses per train of the optical pump laser matched that of the X-rays (564 kHz), with every other X-ray pulse train being optically pumped, i.e. 5 Hz inter-train rate was set for the optical laser (Fig. 1). The complete results of the experiment are reported elsewhere [40] while the details of the optimization and data reduction procedures are presented in the following sections.

3. Optimization of X-ray intra-train repetition rate

When focused tightly at the interaction point both the X-ray and optical laser pulses can perturb or even completely destroy the thin liquid jets used for sample delivery [41,42]. At moderate optical excitation conditions even the probe X-ray pulses alone with typical flux up to 10^{31} photons s^{-1}cm^{-2} may destroy the sample. Due to the femtosecond pulse duration, the sample degradation has minor to no effect on the detected radiation of that pulse after the interaction [43–45], at least within the typical 10^{16} Wcm^{-2} X-ray peak intensity regime used at FXE. However, when working at MHz repetition rates, the sample perturbation may have insufficient time to relax by the time of next pump-probe event and the probed sample volume has to be fully replenished between subsequent probe pulses, i.e., on a time scale of the order of 1 μs. Selection of the optimal X-ray repetition rate should therefore be carefully evaluated for a specific experiment.

X-ray-induced jet perturbation effects are straightforward to monitor when using pulse-resolved MHz frame-rate detectors to collect the probe signals or when a synchronized high-speed camera is available. A different approach is required to monitor jet perturbations when using a detector that is not capable of separating individual probe pulses within a MHz train. One possible approach is demonstrated in Fig. 2. A set of static XES measurements was performed using only two X-ray pulses per train with different temporal spacing (i.e. at different pulse repetition rates) and for different jet flow rates. The incoming intensity of the X-ray pulses was systematically varied using Si and CVD diamond attenuator foils to detect the intensity threshold where the jet perturbations start to affect the detected signal. The total integrated XES signal is plotted as a function of the total incident flux (I_0) measured using a calibrated pin-diode, 3000 images were used to produce each plot. In an ideal case such dependence should be monotonic and

linear. If the first pulse perturbs or destroys the liquid jet and/or the jet speed is not sufficient to fully replenish the liquid sample, the second pulse will interact with a reduced sample volume, thus resulting in a lower total X-ray emission signal for a given I_0 value. This behavior is clearly visible in Fig. 2 (a–d). Fig. 2-a corresponds to the standard FXE setting for pump-probe XES measurements, i.e. 564 kHz pulse repetition rate and 30 mL/min jet flow rate, which respectively correspond to 1.77 μs pulse spacing and ca. 60 m/s linear jet speed. For this setting the total XES signal scales linearly with I_0 which confirms that the probed sample volume is replenished by the arrival of the next probe pulse. Reducing the flow rate to 15 mL/min (linear speed of ca. 30 m/s) leads to the second pulse interacting with the sample region partially affected by the first pulse in the train. Fig. 2-b exhibits a clear "cutoff" I_0 value, above which total XES signal is reduced by approx. 20%. Assuming that both pulses have identical intensity, this value corresponds to a 40% reduction in sample volume, probed by the second pulse in the train. A similar behavior is observed when the pulse repetition rate is increased to 1.1 MHz and 2.2 MHz (Fig. 2-c and d) while the jet flow rate is kept constant at 30 mL/min. Interestingly, reducing the jet flow speed by a factor of 2 does not result in a behavior identical to increasing the pulse repetition rate by a factor of 2, which highlights the complex character of the interaction and jet destruction process.

Further ongoing development of 3D printed nozzles with conical capillary tips (CCT) [46] suitable for Rayleigh jets will provide faster cylindrical and also flat jets with linear speed of up to 120 m/s thus increasing the accessible pulse repetition rate of the experiment to 1.1 MHz while avoiding the jet perturbation effects.

4. Characterization of detector response in the gain-switching region

The gain switching capability of the JF detector enables concurrently high sensitivity and high dynamic range detection. Each pixel has three gain stages and the switching between the stages occurs automatically for each individual pixel, depending on the total accumulated charge for a given pixel.

The detector is designed to have a linear response within each gain stage. Since the JF is a charge integrating detector, converting raw detector output in analog-to-digital units (ADU) into keV or number of photons requires 6 parameters for each pixel: namely, one offset and one gain value per gain stage. In order to produce the final calibrated image, each pixel is corrected depending on its specific gain stage by subtracting the respective offset from the raw signal and by dividing the result over the corresponding gain factor. The offset values are extracted by programmed force switching of the detector into each gain stage and acquiring "dark" images for the same conditions as during the data collection. The specific procedure for determining the absolute and relative gain factors is more involved and can be performed using calibration to a known energy or using a calibrated reference detector [37,47,48]. In brief, for the JF modules used in this study, the original absolute linear gain factors of the high gain stage (G0) were extracted from each pixel from fitting photon peaks produced by weak Cu fluorescence radiation. The original linear gain factors for the other two gain stages G1 and G2 were determined purely electronically from respective charge injection scans. It is crucial to have precisely defined calibration parameters, especially when detecting small sub-percent level changes in the signal strength, as typically done in pump-probe experiments.

4.1. Observation of gain switching artifacts

Simultaneous detection of several X-ray emission lines with a dispersive spectrometer and the JF detector can be used to assess the pixel response and the linearity with intense beam when the signals trigger gain switching. Provided that the sample integrity is controlled
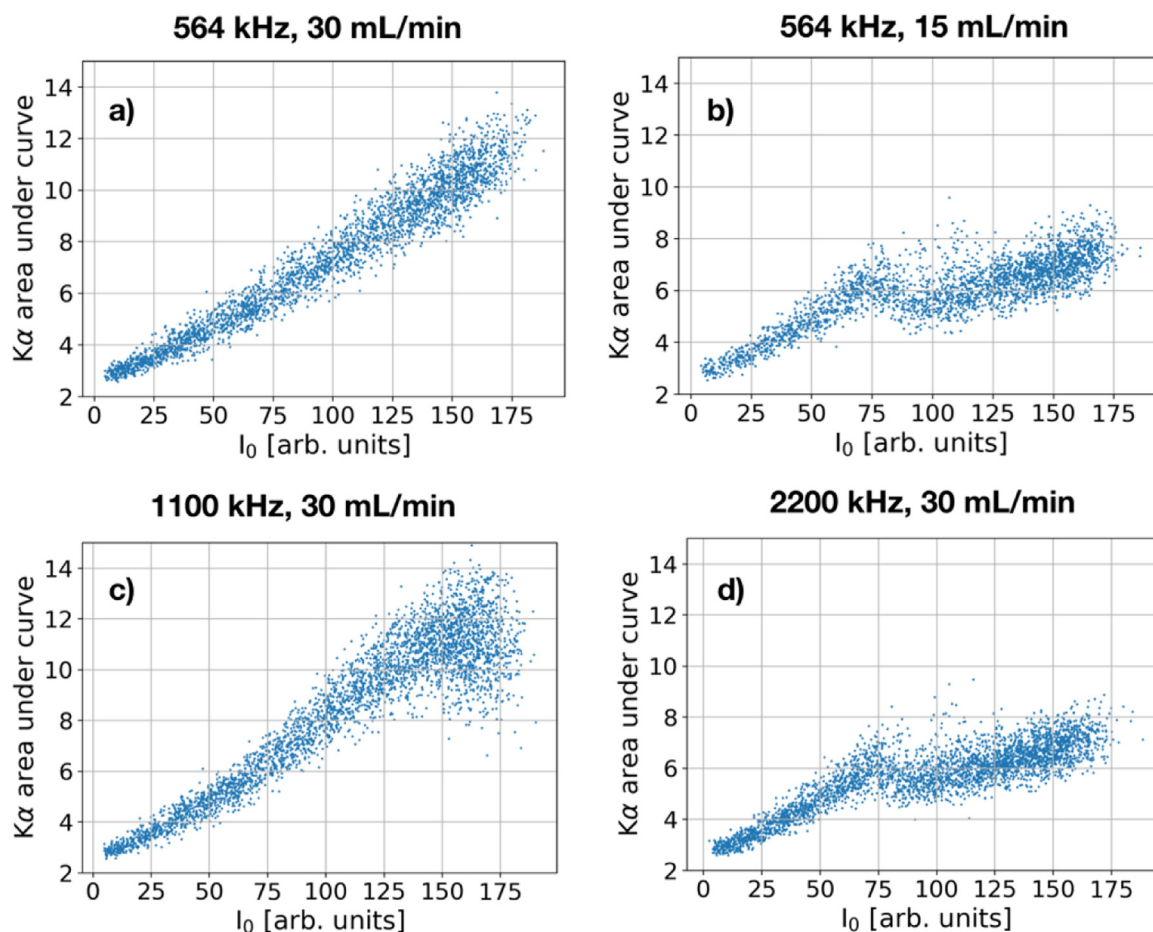
Fig. 2. Optimization of the MHz pulse repetition rate set in an experiment using the integrating JF detector for XES signal collection. All measurements were performed with only two X-ray pulses per train and 100 μm diameter cylindrical liquid jet. Each plot is produced from a total of 3000 images or 5 min of data acquisition. (a) Pulse repetition rate 564 kHz, jet flow rate 30 mL/min (b) Pulse repetition rate 564 kHz, jet flow rate 15 mL/min (c) Pulse repetition rate 1100 kHz, jet flow rate 30 mL/min, (d) Pulse repetition rate 2200 kHz, jet flow rate 30 mL/min.

as described above, the X-ray emission signals depend linearly on the incident flux at all fluencies reachable at the FXE instrument.

We simultaneously recorded a set of static Co $K\alpha_{1,2}$ and Co $K\beta_{1,3}$ X-ray emission spectra for the 10 mM $[Co(terpy)_2]^{2+}$ aqueous solution over a broad range of incoming X-ray pulse intensities that was varied by inserting Si and CVD diamond attenuator foils of different thicknesses. The sample jet flow rate and pulse repetition rate were chosen to ensure that the sample was fully replenished between subsequent X-ray pulses.

An average image containing the $K\alpha_{1,2}$ spectrum is shown in Fig. 3-a. The arrows indicate the pixels chosen to produce the intensity correlation of the $K\alpha_1$ and $K\alpha_2$ lines, as presented in Fig. 3b.

The measured $K\alpha_1$ to $K\alpha_2$ intensity correlation does not behave linearly at the transition of the high (G0) to the medium (G1) gain stage. Three distinct groups of data points can be identified, depending on the gain stage of the two selected pixels:

1. Both $K\alpha_1$ and $K\alpha_2$ pixels are in the high gain stage (G0);
2. The $K\alpha_1$ pixel switches to the medium gain stage (G1);
3. Both $K\alpha_1$ and $K\alpha_2$ pixels switch into the medium gain (G1) stage.

While the $K\alpha_1$ to $K\alpha_2$ intensity correlation seems linear when both pixels are in the same gain stage, it changes abruptly as the gain of one of the pixels changes.

In order to correct the signal artifact at the interface between the high and medium gain stages, a correlation between the $K\alpha$ pixel values with reference to the $K\beta$ ones is introduced. For this, we use the integral intensity of the simultaneously detected $K\beta_{1,3}$ emission line as

the incoming intensity reference (I_0). Since the $K\beta$ emission is weaker than the $K\alpha$ emission by a factor of $\sim$20, it never saturates the high gain stage of JF in a broad range of incident fluencies. Hence, it can be used as an internal reference, that presents the added advantage of being intrinsically normalized to possible slow changes in the jet thickness and sample concentration that influence the detected XES signal. The intensity response of the selected $K\alpha_1$ pixel as a function of the incoming X-ray pulse intensity reference I_0 is shown in Fig. 4. Three issues become evident as additionally highlighted by the linear fits of signals in two gain stages:

(1) The calibrated pixel response changes abruptly as the pixel switches from high to medium gain, indicating a potential shift in the offset of the medium gain;
(2) Different slopes for both gain stages, indicating that the gain values need to be adjusted;
(3) Nonlinear behavior in the medium gain around the gain switching region.

The observed artifacts can be potentially attributed to a drift of the offset due to high total charge in the exposed region of the detector or temperature-induced effects in the sensor.

4.2. Effect the detection artifacts on the XES spectral line shapes

The artifacts shown in Fig. 4 affect the static and transient measured XES spectral line shapes. Data subsets were compared based on their I_0 and data statistics for individual gain stages. A histogram of recorded I_0
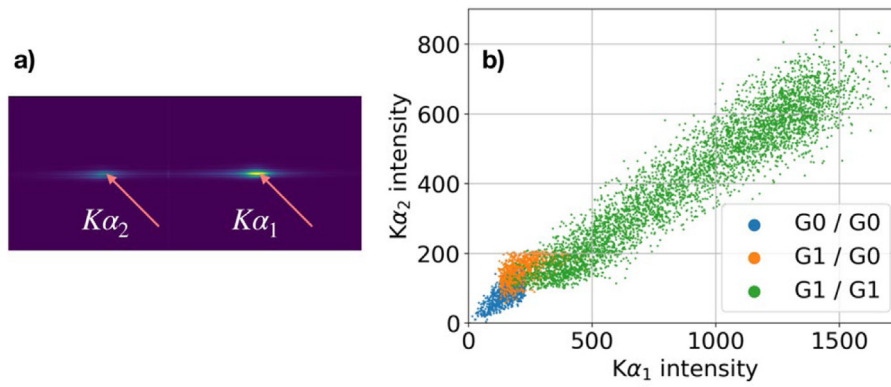
Fig. 3. (a) JF image of simultaneously detected Co $K\alpha_1$ and $K\alpha_2$ emission lines. Arrows indicate pixels from $K\alpha_1$ and $K\alpha_2$ regions selected for intensity correlation. (b) Correlation of $K\alpha_1$ to $K\alpha_2$ signals in units of keV. Different combination of gain stages of both pixels depicted by different colors. As can be seen, when both pixels are in the same gain stage (G0/ G0) or (G1/ G1) the intensity correlation is linear, however a discontinuity appears as one of the pixels switches its gain stage.
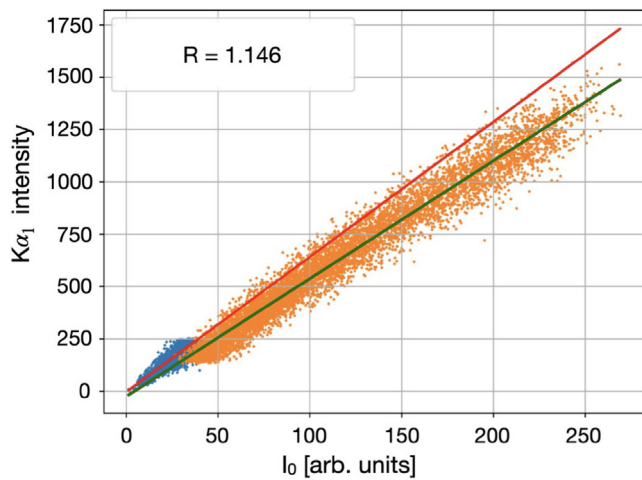

Fig. 4. Dependence of the intensity of the $K\alpha_1$ pixel versus reference incident flux, extracted as the integral intensity of the simultaneously measured $K\beta_{1,3}$ line. Blue – high gain (G0), orange – medium gain (G1). Red and green lines show corresponding line fits. Range of I_0 intensities for which both gains coexist are excluded from the fits.

values is shown in Fig. 5-a. Different colors highlight four regions of I_0 distribution that were selected to calculate the corresponding average Co $K\alpha$ XES spectra in Fig. 5-b. The spectral line shapes were extracted from integration over 12 pixels in the non-dispersive direction (vertical direction in Fig. 3-a) and then normalized to the total integrated intensity over the whole spectrum. The following groups of JF images were selected for extraction and averaging of the spectra:

"Default gain": Images where all pixels of the detector are in the G0 gain stage,

Subset 1 *"from 0 to 10%"*: subsets of images with the 10% lowest I_0 signal, but where at least one pixel over the spectrum switched gain to the medium stage;

Subset 2 *"from 30 to 40%"*: subsets of 10% images with I_0 signal values between 30th to 40th percentile and where at least one pixel over the spectrum switched gain to the medium stage;

Subset 3 *"from 90 to 100%"*: subsets of images with 10% highest I_0 signal values and where at least one pixel over the spectrum switched gain to the medium stage.

Subset 1 contains images where only few pixels around the peak of the $K\alpha_1$ emission line switched gain and therefore is most sensitive to the discontinuity that occurs upon gain switching. This is reflected in a characteristic "dip" in the maximum of the $K\alpha_1$ peak (Fig. 5-b, orange trace), relative to the reference spectrum (Fig. 5-b, blue trace).
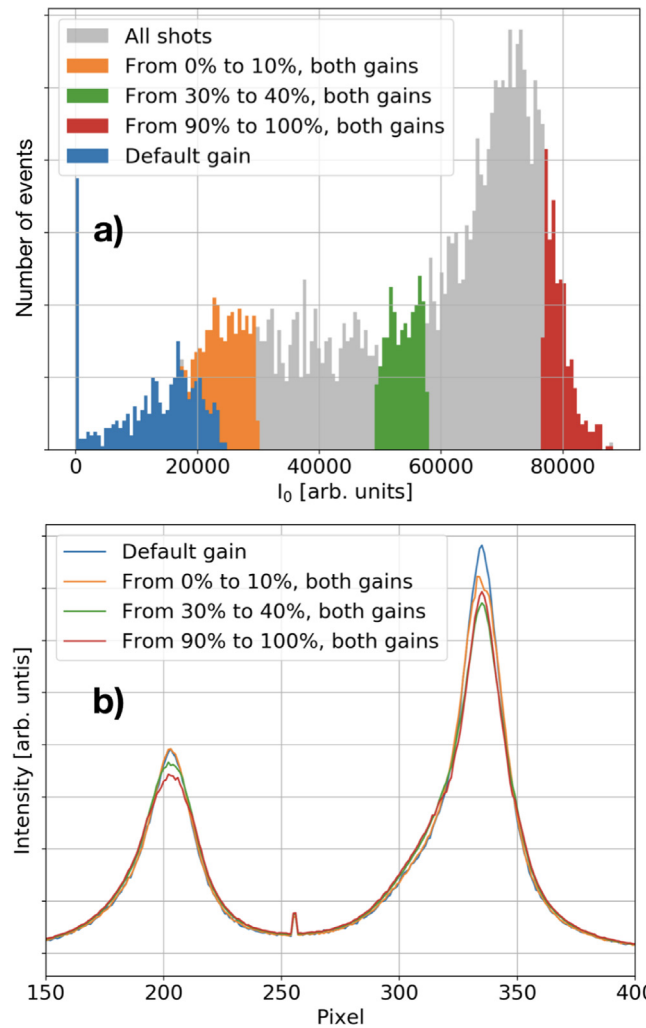

Fig. 5. (a) Distribution of I_0 for recorded Co $K\alpha_{1,2}$ XES spectra. Colors highlight parts of the distribution, selected to make plots in panel (b).

Subset 2 contains images with higher signal levels, in which the gain switches for a larger number of pixels in a broader area around the peak of $K\alpha_1$ line, but with the $K\alpha_2$ still being within the high gain stage. Therefore, *subset 2* represents both the discontinuity artifacts due to inaccurate gain switching correction and the misalignment of gain stage factors. The $K\alpha_1$ versus I_0 correlation shown in Fig. 4 presents data
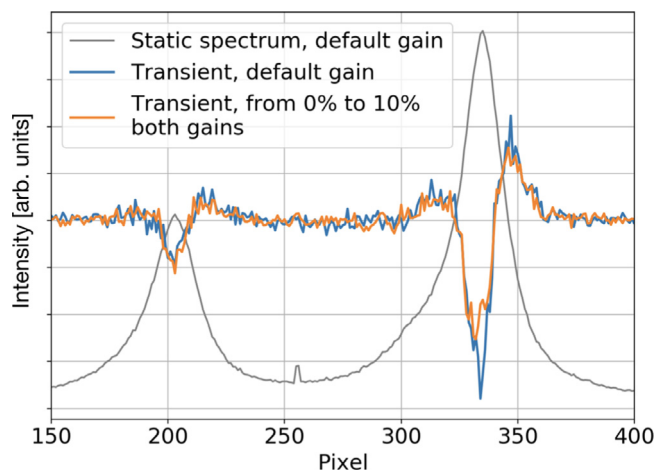
Fig. 6. Laser ON — Laser OFF XES signals for a 100 fs pump-probe delay, extracted only from the images entirely in the default gain (blue) and from 10% of the weakest images where at least one pixel switched gain (orange). Gray — static spectrum taken from images fully in the default G0 gain stage.

taken from subset 2. Pixels that exceed the gain switching threshold appear to have lower ADU values compared to the case if the gain stages of all pixels were correctly aligned. This results in the $K\alpha_1$ line appearing vertically compressed with respect to the $K\alpha_2$ for this subset of spectra, so the intensity ratio of $K\alpha_1/K\alpha_2$ is not maintained.

Subset 3 contains images in which the incident flux was high enough to trigger switching to the medium gain in most of the pixels around both $K\alpha_1$ and $K\alpha_2$ lines (Fig. 5-b, red trace). This leads to the strongest distortions in the XES line shapes, with both $K\alpha_1$ and $K\alpha_2$ emission peaks appearing broader and vertically compressed.

Finally, the resulting nonlinear response of the detector also affects laser-induced pump-probe difference signals. Fig. 6 compares the reference Laser ON — Laser OFF difference XES signal calculated from images entirely in the defaults G0 gain stage (blue curve) to that calculated using the 10% weakest gain-switched image pairs (orange curve). It is evident that the transient signal of the gain switched images significantly deviates from the reference signal around the maximum of $K\alpha_1$ peak, where the pixels with switched gain stage are localized. In measurements with weak difference signals, meaning the spectral shapes and respective detector images for the Laser ON and Laser OFF spectra are not very different, the nonlinearity distorts both the Laser ON and OFF spectra in a similar way. This makes the pump-probe difference spectrum appear less affected by the detection artifacts compared to the static XES spectra themselves. However, in measurements where Laser ON spectrum differs significantly from the Laser OFF, or if there is a systematic difference in the total strength of laser-pumped and unpumped spectra, the contribution of distorted spectral components due to detector nonlinearities accumulate and may start dominating the pump-probe difference curves. Systematic variation of the signal strengths with and without laser excitation may occur e.g. due to accumulated thermal expansion or partial destruction of the liquid jet by laser pump pulses.

5. Internal correction of gain switching artifacts

Different approaches can be implemented for correcting the JF detector artifacts in XES data. We use a dataset of $K\alpha_{1,2}$ pump-probe XES from the 10 mM $[Co(terpy)_2]^{2+}$ solution as above recorded at relatively high incident X-ray flux. The dataset contains 6177 images, out of which only 143 are entirely in the default high gain stage (G0) of the detector. The following approaches are described below:

(1) Image-based filtering;
(2) Pixel-based filtering;
(3) Pixel-based filtering with gain alignment.

5.1. Image-based filtering

The most straightforward method to correct the data for the detector nonlinearities is to simply discard all images in which gain switching has occurred in at least in one pixel. Although this image-based filtering approach delivers data free from any gain switching or gain misalignment artifacts, it can give exploitable results only when a small percentage of images have experienced gain switching. Otherwise it leads to significant data decrease in the amount of data used and thus much poorer overall statistics. For example, in the considered dataset almost 98% of the images would have to be filtered out. Fig. 7 demonstrates the results of such an image-based filtering approach, applied to the selected XES data set: Fig. 7-a displays the static spectrum, Fig. 7-b shows the Laser ON - Laser OFF difference trace. In the following, the image-based filter will be used as a benchmark for other data treatment approaches.

5.2. Pixel-based filtering

A more refined method for correcting the spectral artifacts relies on the concept of pixel-based filtering, which takes advantage of the fact that pixels in the JF detector switch gain stages independently. In this approach, the pixels that have switched gain stage in a given image are masked out by the filtering routine, thus producing a dynamic intensity-dependent pixel mask on a per-image basis. The final averaged image is then formed from the fractions of images, containing only the pixels in the high gain, and each partial image is respectively normalized by I_0 before averaging.

The pixel-based filtering approach is schematically illustrated in Fig. 8, where panels (a)–(e) are masked images of the $K\alpha_1$ region, panel (f) is the final image, produced by averaging masked images and normalized to I_0. Fig. 8-g additionally shows the number of images contributing to each pixel of the average image in (f). It is worth noting that precise determination of I_0 for each image is crucial, since it brings pixels of masked images to the same relative scale allowing for subsequent averaging without distortions. Each pixel of the final average image results from a different number of individual points contributing to it, with pixels in the stronger parts of the image having less statistics compared to the pixels in the weaker parts. Compared to the image-based filtering the pixel-based filtering method significantly improves the signal quality for all pixels by utilizing more images to compose the final average spectrum, which is particularly noticeable in the pixels detecting weaker signals where the SNR is intrinsically lower.

As a generalization, instead of relying on an I_0 source based on another region of each image or signals from a different detector, the following self-referenced procedure can alternatively be used. The filtering routine loops through all masked images in the dataset and forms a mask of common pixels with signal above the elastic scattering background level defined from a neighboring region away from the emission spectrum. As a result, the pixels always staying in high gain state and present in all images of the dataset can be isolated. The total integral signal from these pixels, common for all masked images, is used as per-image I_0 to which the individual images are normalized before averaging. This step automatically ensures that all masked images are brought to the same intensity scale.

The advantage of the pixel-based filtering approach is further demonstrated in Fig. 9. The static Laser OFF Co $K\alpha_{1,2}$ XES line shape, extracted with the pixel-based filtering approach, matches well the reference one obtained with the image-based filtering method (Fig. 9-a), however with improved statistics. The agreement confirms the applicability of both the pixel-filtering approach and the self-referencing procedure for I_0 extraction, since incorrect per-image I_0 normalization would result in a distorted spectral line shape.

The significant improvement in the SNR over the image-filtering method is demonstrated by Fig. 9-b. The improvement is especially
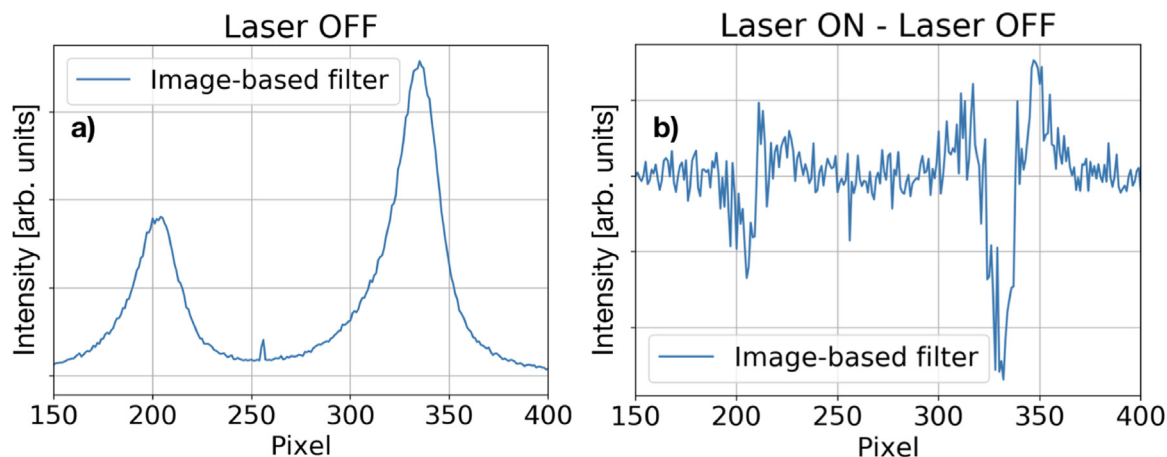
Fig. 7. Image-based filtering approach. (a) Laser OFF static XES spectrum, (b) Corresponding Laser ON - Laser OFF difference trace. The limited SNR is due to the fact that only a small fraction of all collected images (143 out of 6177) could be used after applying the image-based filtering method.
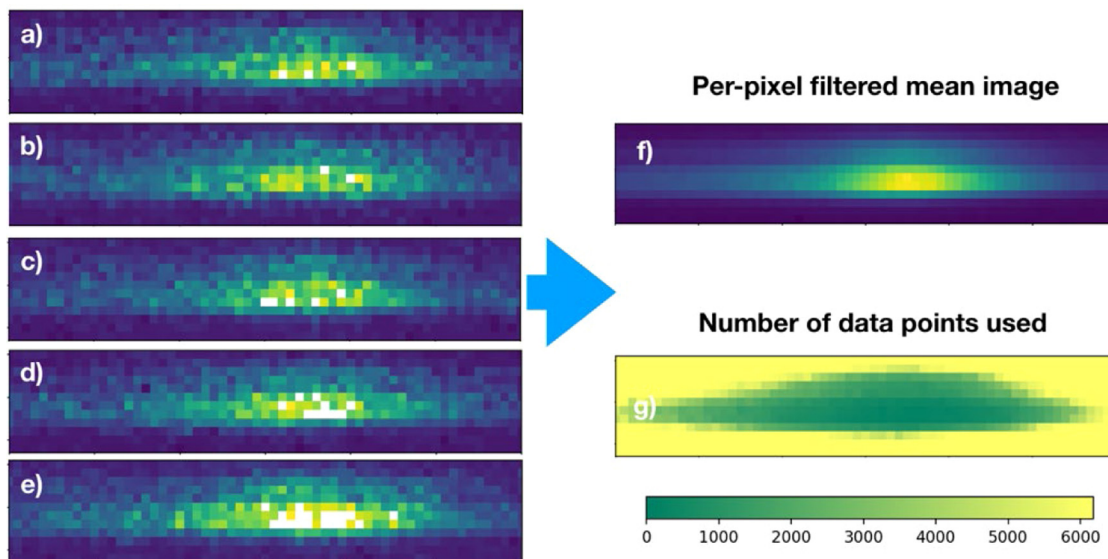

Fig. 8. Pixel-filtering approach. (a)–(e) JF Co Kα_1 pixels that switched gain are masked out and shown with white color in the images, I_0 increases from (a) to (e), (f) is the resulting mean Kα_1 image, produced by averaging masked images, normalized to I_0, (g) – number of data points contributing to per-pixel filtered mean image, maximum number is 6177 (yellow color)..
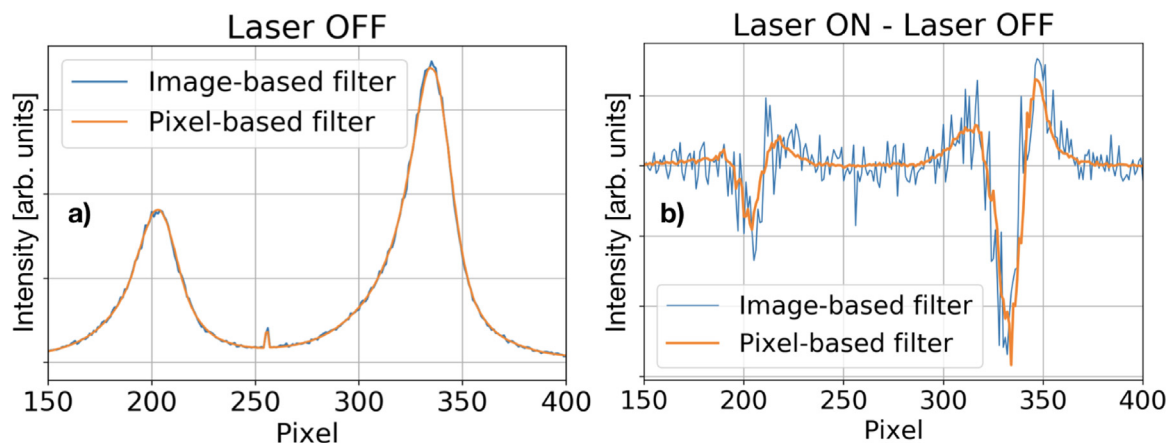

Fig. 9. Comparison of the performances of the image-based and pixel-based filtering approaches: (a) Laser OFF static Co K$\alpha_{1,2}$ spectra, (b) respective Laser ON - Laser OFF difference traces.

noticeable for the pixel regions exposed to weak XES signals. In contrast to the image-based filtering, almost all images of the dataset are included in the final image to compose the spectrum. Some residual noise spikes are still present in the difference signal area around the $K\alpha_{1,2}$ peaks maxima. This is due to fewer data used for the final filtered image and spectrum since the maximum signal pixels undergo the gain stage switching more often in the course of extended acquisition with fluctuating pulse intensity of XFEL.

5.3. Pixel-based filtering with gain alignment

The performance of the pixel-based filter can be further improved when it is combined with the gain factor alignment procedure, similar to the one performed during the initial detector calibration. The idea of the gain alignment procedure is to "align" the data points of pixel signal intensities plotted as a function of the incoming intensity (I_0) in the medium and low gain stages to the data points in the high gain stage. As a result, the gain switching discontinuities are eliminated and the detector intensity response is linearized over the entire combined dynamic range. This procedure also eliminates the need for independently obtained offset values and gain constants for medium and low gain stages, allowing to convert ADU to keV using offset values and gain constants for the high gain stage only. The gain constants for the high gain stage can be obtained by measuring single photons with known energy and fitting positions of the photon peaks, while offsets are obtained by collecting images without any X-ray exposure. However, the X-ray signal-based gain alignment procedure cannot be applied to all pixels unless the following requirements are fulfilled:

(1) The measurement is taken with varying signal intensities to be able to sample pixels response in different gain stages;
(2) Enough data is available in all the gain stages to allow performing a reliable linear fit for each pixel. Data points that fall in the I_0 region where both gains coexist have to be excluded from the fit.

Condition (1) is usually partially met at a SASE-based XFEL source due to the stochastic nature of its radiation. In addition, in case when a cylindrical liquid jet is used, pointing fluctuations result in X-ray pulses probing parts of the liquid jet of slightly different thickness, further amplifying variations in signal intensity conditions. Condition (2) is implemented in our gain alignment algorithm by requiring that for a given pixel:

$$I_0^{max}(G1) - I_0^{min}(G1) \geq I_0^{max}(G0) - I_0^{min}(G0)$$

Where $I_0^{max}(G1)$, $I_0^{min}(G1)$, $I_0^{max}(G0)$, $I_0^{min}(G0)$ are the maximum and minimum I_0 values at which the pixel was in the medium gain stage (G1) and high gain stage (G0), respectively. In other words, we require that the pixel response in G1 stage is probed in the range of at least the same width of I_0 values, as for the default G0 stage.

If a given pixel satisfies conditions (1) and (2), its data in the medium gain is aligned to the high gain stage according to equation:

$$I_{corr}(G1) = [I(G1) - offset(G1)] * \frac{slope(G0)}{slope(G0)} + offset(G0)$$

Where $I(G1)$ is the non-corrected pixel signal in stage G1, $slope(G0)$, $offset(G0)$, $slope(G1)$, $offset(G1)$ are parameters of the line fits to the data points in stage G0 and G1 respectively.

The result of the gain alignment procedure applied to three selected pixels, exposed to different XES signal levels is presented in Fig. 10. Pixel 1 (Fig. 10a–d) is an example of pixel for which condition (2) is not fulfilled — data points in G1 stage are not exceeding the I_0 region where gain uncertainly exists and reliable fitting cannot be performed. Excellent results are achieved for pixels 2 and 3 (Fig. 10-b, c, e, f) — the pixel response is linear with no gap between G0 and G1 stages. A slight deviation from the linear behavior around the gain switching region is visible for pixel 3 as the straight line does not fully represent

the data points of G1 stage for the weakest signals, which is similar to the pixel response presented in Fig. 3. This issue can be observed when the pixel response is probed deep into the medium gain stage (G1). Second order polynomial fitting would be required to correct this type of nonlinearity, but as we demonstrate further, the effect on the resulting XES spectra remains below our detection uncertainty limit.

While the per-pixel filtering approach allows efficient use of the pixels exposed to the weak signal levels, for which the gain switching happens less frequently, the gain alignment procedure allows using data from the pixels exposed to medium and strong signal levels, for which statistics are sufficient for performing reliable gain alignment. The combination of these approaches allows producing high data quality and correcting the XES line shapes, even though gain switching artifacts may be present in the original dataset.

The complete procedure of the pixel-based filtering with gain factor alignment consists of the following steps:

i Formation of a mask that defines the pixels fulfilling conditions (1) and (2) for gain alignment;
ii Per-pixel gain factor alignment;
iii Application of the pixel-based filtering to the gain-aligned images.

Fig. 11 compares the static Laser OFF XES Co $K\alpha_{1,2}$ spectra extracted by three the data filtering methods along with the analysis of their Standard Error of the Mean (SEM). As can be seen from Fig. 11-a, the XES line shape extracted with the pixel-based filter with gain alignment overlaps perfectly with the reference from the most conservative image-based filter. This confirms that the gain factor alignment procedure works as expected, eliminating intensity discontinuities upon gain switching and correcting the gain factors in the medium gain region. Moreover, it indicates that the mentioned nonlinear behavior around the gain switching region for pixels detecting XES signals that reach deep into medium gain, does not cause any visible distortions in the spectra.

Fig. 11. b demonstrates the significant improvement in the SNR of XES spectra after applying the additional gain factor alignment procedure. The traces show the SNR for the Laser OFF spectrum, obtained with the filtering approaches described above. The pixel-based filter provides up to 18x improvement of the SEM value, however its performance becomes limited in the areas around the Co $K\alpha_{1,2}$ peak maxima, where the XES signals are the strongest and where many data points are masked out due to the gain switching. The combination of the pixel-based filtering with gain factor alignment compensates for that limitation, allowing to retrieve additional data and improve the signal quality where pixel response could be linearized. The impact of the gain alignment procedure in the signal quality is clearly seen in Fig. 11-b. The shaded areas indicate the segments where the response of at least one pixel in the region of interest (ROI) on the detector is corrected for the gain nonlinearity. Within these areas, the pixel-based filter with gain factor alignment provides up to 3.5x smaller uncertainties compared to the pixel-based filtering alone, while allowing almost all of the image data points to be used. In the areas outside of the shaded regions, both filtering approaches provide nearly identical signal quality, as expected, since no gain switching has occurred.

Fig. 12 presents the Laser ON - Laser OFF difference signals extracted using the pixel-based filter with gain factor alignment compared to the conservative image-based filter. The signal quality is substantially improved for all pixels, in accordance with SEM improvement ratio, presented in Fig. 11-b.

Femtosecond pump-probe experiments are conducted to investigate dynamics of ultrafast processes and therefore the pump-probe delay needs to be varied over a certain range. To further demonstrate the advantage of the filtering approaches in improving the signal quality we apply the approaches described above to a delay scan of the $[Co(terpy)_2]^{2+}$ aqueous solution, recorded with 600 frames per scan point, i.e. one minute of data acquisition at FXE. As a figure-of-merit
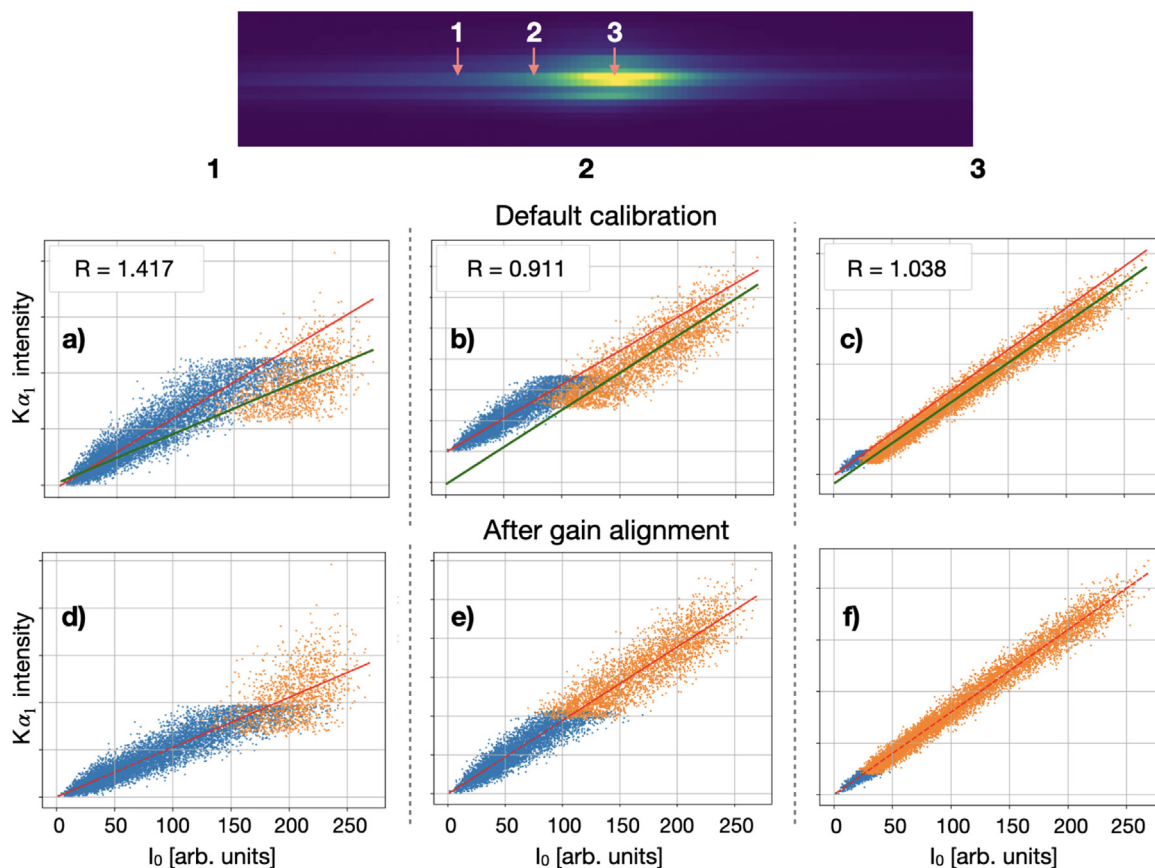
Fig. 10. Pixel-filtering with gain alignment approach. The result of the gain factor alignment and offset correction for pixels exposed to different levels of incident flux, I_0. (top row) Average image of the Co $K\alpha_1$ emission line. The arrows indicate three pixels selected for comparison, representing weak (1), intermediate (2) and strong (3) signals. (a–c) Initial pixel response after the standard calibration routine illustrating the presence of artifacts in both offset correction and gain factor for all cases. The red and green lines represent linear fits for the two gain stages. (d–f) Result of refined gain factor alignment and offset correction in the pixel response. (d) The presence of artifacts is greatly reduced, but still exists in the region of gain transition (around 150–200 a.u. in I_0) due to insufficient data points of pixel signals in G1 stage. (e,f) Excellent alignment of pedestals and gain factors. (f) Slight nonlinearity in the response in G1 gain stage is present around the gain switching region.
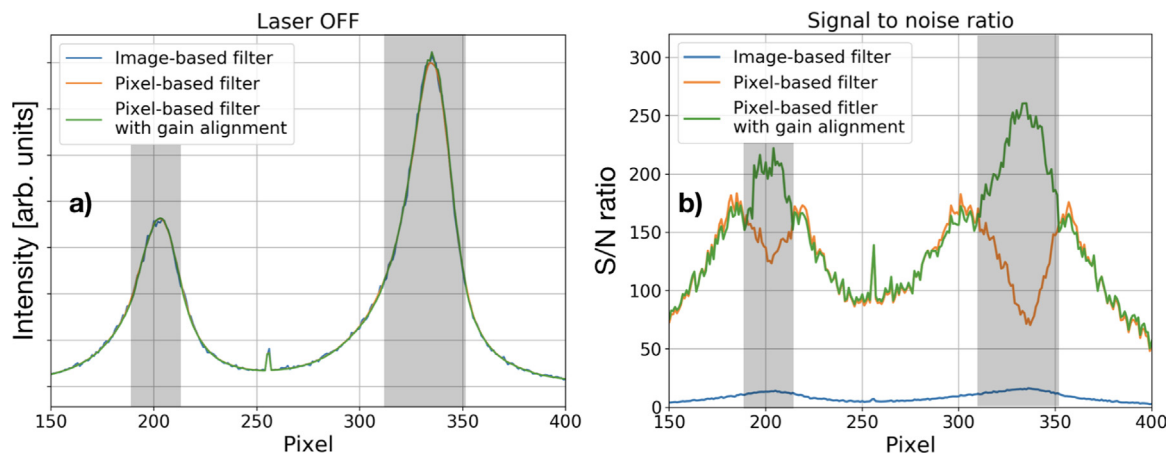

Fig. 11. Performance of Pixel-based filter with gain alignment. Shaded areas highlight pixels, where at least one pixel in the region of interest (ROI) of the detector experienced gain alignment: (a) static Laser OFF spectra, (b) improvement of SNR for the Laser OFF spectrum obtained with pixel-based filter with gain alignment.

(FOM) for the strengths of the pump-probe signal, we use the integrated intensity of the transient difference signal at the Co $K\alpha_1$ emission line, specifically in the pixel region [300, 360]. This dataset in the considered region suffers from the same gain switching issues and nonlinearities as the data presented in Fig. 3. This means that only around 11% of all images are fully in the high gain stage, corresponding to only 60–70 entirely linear images for each delay point. Two kinetic

traces, extracted using the image-based filter and the pixel-filter with gain alignment are presented in Fig. 13. The blue and gray shaded areas represent the confidence interval (+/−1 SEM) for the FOM values, extracted using the conservative images-based filter and the pixel-based with gain factor alignment filter, respectively. Both traces are offset to have mean value zero before time-zero and normalized to unity. As can be seen, the pixel-based filter with gain factor alignment results in a
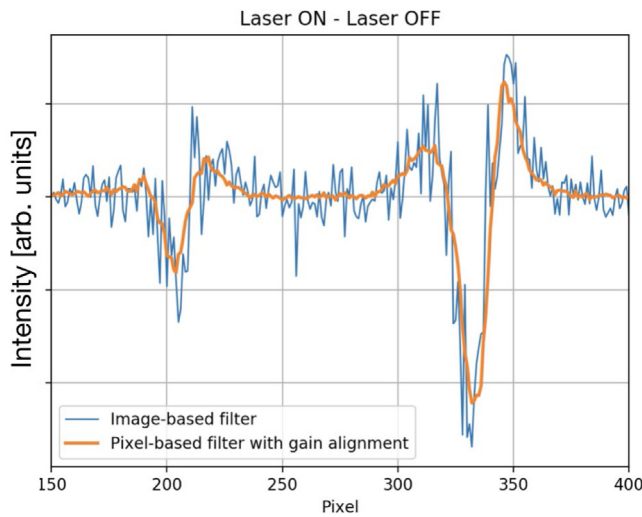
Fig. 12. Substantial improvement in the quality of Laser ON - Laser OFF XES difference signal offered by the pixel-based filter with gain factor alignment, relative to the conservative image-based filter.
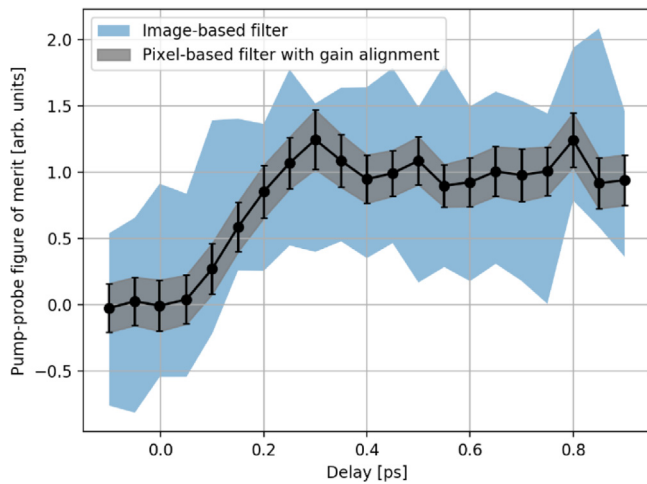

Fig. 13. Substantial improvement in the signal quality of the XES kinetics trace, provided by the pixel-based filter with gain alignment over the image-based filter. The shaded areas represent the confidence intervals for the kinetics traces. Blue – baseline image-based filter, gray – pixel-based filter with gain alignment.

much clearer kinetic trace with well-defined step-like profile and much higher SNR.

6. On using low framerate detection for MHz-rate pulse trains

The MHz repetition rate at the European XFEL enables high average X-ray photon flux and thus high signal quality even in photon-demanding types of experiments such as XES on dilute solutions. High dynamic range and low noise novel 2D detectors for hard X-rays like the JF [34] or the ePix [36] are limited by their frame rate and, therefore, at a MHz source, signals from several X-ray pulses are accumulated in a single exposure image thus potentially reaching the dynamic range limits. MHz frame rate and multiple gain-stage detectors like the Gotthard [49,50], the DSSC [51,52], the AGIPD [53–55] and the LPD [56–58] are custom designed for operation at MHz rate XFEL sources. Such detectors offer single-shot detection capabilities enabling pulse-resolved diagnostics for the intrinsically fluctuating radiation of individual X-ray pulses. Burst-mode operation of the source, as at European XFEL, provides various possibilities for per-burst accelerator

feedbacks thus improving the overall radiation stability within the trains of pulses. In this case the advantage of pulse-resolved detection may not lead directly to improved data quality for low signal levels such as XES on dilute solutions. This is especially the case for MHz framerate detectors due to intrinsically high noise and effects of short- and long-term instabilities related to the typically burst mode of operation and limitations of fast readout electronics. In addition to varying heat load and collected charge in the detector over a pulse train, the burst mode of readout is usually enabled by on-chip memory that requires a relatively large pixel and thus higher input capacitance, increasing the leakage current fluctuations at very short sub-microsecond exposures.

To compare potential performance of a MHz-rate single-shot detector over the train-integrating 10 Hz rate JF detector for pump-probe XES signals at FXE, we use the static and difference XES curves extracted from the experimental results presented above. Fig. 14-a shows a typical Co K$\alpha_{1,2}$ spectrum and its pump-probe difference at 100 fs delay in units of Co Kα photons (ca. 6.9 keV) per pixel scaled to a single X-ray pulse. The number of photons per pixel was deduced from the image signal using a gain conversion factor which was extracted from a separate calibration measurement of photon peaks from Cu Kα fluorescence [47]. Under typical experimental conditions for solution-phase XES, photon flux barely approaches 1 photon per pixel per pulse even at the peak of the strongest Co Kα_1 emission line. At such signal level, it is challenging to overpower the overall pixel noise and detection instability in each individual single-shot image. This is particularly relevant considering that the measured signal of interest is the pump-probe difference between spectra with and without the laser excitation. The actual difference signal is at about 26 times lower in amplitude compared to the static spectrum. For the weaker Co Kβ emission spectrum both the number of photons in the static spectrum and the relative strength of the pump-probe difference signal become even smaller as plotted in Fig. 14-b.

To compare the estimated SNR of train-integrating ("slow") and pulse-resolved ("fast") detection approaches we consider the main sources of noise, namely the read noise, dark noise, background noise and photon noise, or shot noise.

For uncorrelated and random noise sources, the SNR can be written as follows:

$$SNR = \frac{S_{XES}}{\sqrt{\sigma^2_{photon} + \sigma^2_{background} + \sigma^2_{dark} + \sigma^2_{read}}}$$

The squared photon noise contribution σ^2_{photon} equals to the signal strength S_{XES}. The background signal in our case originates mostly from the elastically scattered photons of the incident beam. The background can be effectively eliminated by shielding and using He-filled scattering paths and therefore is neglected. The dark noise is proportional to the integration time and can be excluded for the pulse-resolved detection at MHz rate, while it does contribute to the signals integrated over the train length of few hundreds of μs. For the JF detector unit with integration time of 300 μs used in this study, the dark and read noise contributions have similar strengths and approximately result in combined noise of $\sigma_{JF} = \sqrt{\sigma^2_{dark} + \sigma^2_{read}} = 125 \, e^-$ e.n.c. or 0.45 keV RMS. The read noise is the lowest measurable signal in the dynamic range. It originates from the readout electronics and depends on the mode of operation. The read noise contributes to the measured signal regardless of the length of the integration time or the number of photons. Fast readout electronics have relatively higher readout noise than the slower ones. Denoting the XES spectral signal per pulse as S^p_{XES} the estimated SNR from measuring N pulses in a train can be written as follows for the "slow" and "fast" detection, respectively:

$$SNR_{slow} = \frac{N S^p_{XES}}{\sqrt{N S^p_{XES} + \sigma^2_{JF}}}, \tag{1}$$
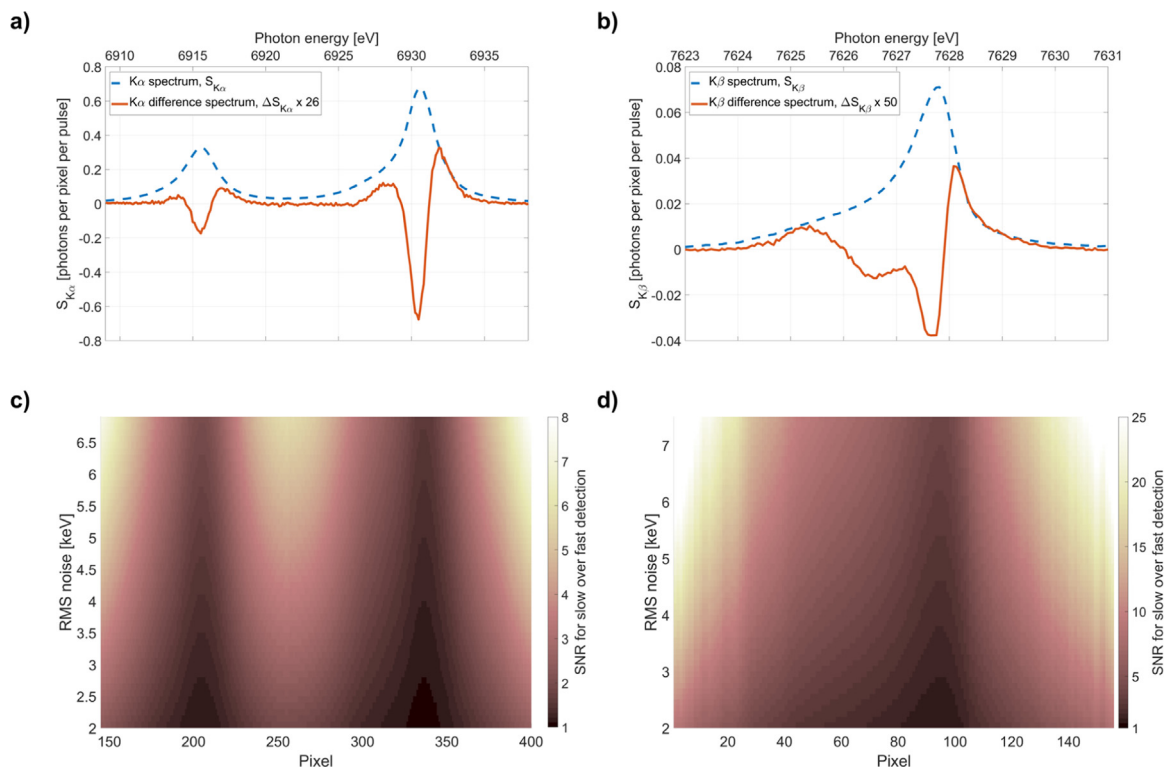
Fig. 14. (a) and (b) Co K$\alpha_{1,2}$ and Co Kβ emission spectra (dashed curves) and the respective pump-probe differences at 100 fs delay (solid curves). The spectra are given in absolute number of photons per detector pixel and the differences are multiplied by factors of 26 and 50 for the Kα and Kβ emission, correspondingly, for better visibility; (c) and (d) relation of SNR for slow over fast detection approaches for the respective spectral signals presented in panels (a) and (b).

$$SNR_{fast} = \frac{NS^p_{XES}}{\sqrt{N(S^p_{XES} + \sigma^2_{read})}}. \tag{2}$$

These expressions highlight the fact that the read noise accumulates for multiple exposures, so that the signal is always limited by the read noise. When a signal from multiple pulses is accumulated in one exposure with single read-out, the detection may become shot-noise limited provided the number of pulses N is sufficiently high.

Typical noise performance of MHz frame rate detectors ranges from ca. 1 keV for the 1D Gotthard-II (237.6 e- e.n.c. RMS) [59] and the 2D AGIPD (301 e- e.n.c. RMS) [53] to about 4 keV RMS for the parallel-gain LPD [56]. In comparison, the JF detector read noise is typically on the order of 100 e- e.n.c. or 360 eV RMS [34], while the more recent chip version reaches 35 e- e.n.c. or 126 eV RMS [35].

Using the expressions (1) and (2) above we estimated the ratio of the SNR performances for the given JF ("slow") detector and a generic MHz rate "fast" detector with increasing read noise. Fig. 14-c demonstrates the relation of SNR for slow over fast detection as a function of RMS read noise of the fast detector estimated for the specific intensity distribution of Co Kα XES. The noise of the slow detector is taken as the JF noise of 0.45 keV RMS, which includes a realistic increase in dark current due to 300 μs exposure required for 150 pulse at 564 kHz. A similar plot for the case of weaker Kβ spectrum is presented in Fig. 14-d. As can be seen the SNR for the low rate (or slow) detection is several times higher than that for the pulse-resolved fast detection, and the advantage becomes further pronounced for very weak signals away from the spectral maxima or for the less intense lines.

The SNR estimations provided in Fig. 14 are applicable primarily to the case of relatively high noise in the pulse-resolved detection, i.e. above 2.3 keV RMS, when single-photon sensitivity at 3σ-level is not reached for the Co K$\alpha_{1,2}$ and Kβ emission photons. It should be noted that the aspect of the pixel size was not considered for the two detection types, and that may improve the performance for

single-shot detection with larger pixels although at the expense of spectral resolution. Additionally, even if single photon discrimination at acceptable level is reached for the high frame rate detectors, a reliable single photon counting analysis may be strongly limited by the presence of weak elastic scattering background from the incoming beam, which is typically close in photon energy to the emission energy itself also in the non-resonant case.

7. Conclusions

In this work, we presented a methodology to identify and mitigate the issues occurring in X-ray emission measurements on fast jets at high-flux high repetition rate X-ray free-electron laser source such as European XFEL.

First, we demonstrated a procedure to detect X-ray induced jet perturbations induced on a MHz time scale, with a low frame rate integrating detector such as the JF, thus enabling a quick and efficient optimization of the experimental conditions in-situ without the need of fast and complex MHz area detectors.

Second, we described data processing methods that allow direct ad-hoc corrections for recovering almost 100% of useful data from the multi-gain stage detector, even when severe gain switching artifacts and nonlinearities are present, without any prior assumptions, restrictions or additional measurements. The proposed methods are highly efficient and do not require significant computing resources. Although the advantages of these methods are demonstrated using the energy-dispersive XES technique, they are general and can be readily applied to other types of image data once a reliable internal signal reference is defined. The image correction functionalities presented in this work are available as a part of Python data processing package developed at FXE.

High average photon flux at MHz repetition rate XFEL facilities, such as European XFEL, provides new opportunities for experiments that are demanding in terms of signal strength as, for example, femtosecond pump-probe XES in dilute solutions. Taking full advantage

of the MHz source radiation requires accordingly high rate sample delivery systems and MHz frame rate detectors with low noise. Under the ideal conditions of sufficiently high sample exchange rate and when measured signals are well above the detector read noise, the pulse-resolved detection at MHz rates helps to overcome the gain saturation and nonlinearity issues while making use of available per-pulse beam diagnostics data. However, such MHz detection typically results in poorer total SNR due to the read noise contributions from the individual single-pulse readout events, especially when the signal strength itself starts to be comparable to the detector noise. In the specific case of burst-mode pulse structure, the combination of MHz repetition rate, radiation stability over the burst duration and of the low frame rate low noise detection matches well the requirements of simultaneous high sensitivity and high dynamic range for pump-probe XES measurements in dilute solutions. Provided that the experimental conditions and beam parameters are well maintained over extended sub-millisecond exposures containing multiple X-ray pulses, as e.g. per train at the European XFEL, and that the integrated signal strength is relatively weak, the use of low noise and low frame rate detectors becomes advantageous.

CRediT authorship contribution statement

M. Biednov: Conceptualization, Methodology, Investigation, Formal analysis, Visualization, Writing – original draft, Writing – review & editing. **H. Yousef:** Methodology, Investigation, Writing – original draft, Writing – review & editing. **F. Otte:** Methodology, Investigation. **T.-K. Choi:** Methodology, Investigation, Writing – review & editing. **Y. Jiang:** Methodology, Investigation. **P. Frankenberger:** Investigation. **M. Knoll:** Investigation. **P. Zalden:** Methodology, Investigation. **M. Ramilli:** Methodology, Investigation, Writing – review & editing. **W. Gawelda:** Conceptualization, Methodology. **S.E. Canton:** Conceptualization, Methodology, Writing – review & editing. **F. Alves Lima:** Methodology, Investigation, Writing – review & editing. **C. Milne:** Conceptualization, Methodology, Writing – review & editing, Supervision. **D. Khakhulin:** Conceptualization, Methodology, Investigation, Project administration, Writing – original draft, Writing – review & editing, Supervision.

Declaration of competing interest

The authors declare that they have no known competing financial interests or personal relationships that could have appeared to influence the work reported in this paper.

Data availability

Data will be made available on request.

Acknowledgments

References

[1] P. Glatzel, U. Bergmann, High resolution 1s core hole X-ray spectroscopy in 3d transition metal complexes—electronic and structural information, Inorg. Chem. 249 (2005) 65–95.

[2] N. Lee, T. Petrenko, U. Bergmann, et al., Probing valence orbital composition with iron Kβ X-ray emission spectroscopy, J. Am. Chem. Soc. 132 (28) (2010) 9715–9727.

[3] Frank de Groot, High-resolution X-ray emission and X-ray absorption spectroscopy, Chem. Rev. 101 (6) (2001) 1779–1808.

[4] U. Bergmann, M.M. Grush, C.R. Horne, et al., Characterization of the mn oxidation states in photosystem II by Kβ X-ray fluorescence spectroscopy, J. Phys. Chem. B 102 (42) (1998) 8350–8352.

[5] I. Zaharieva, P. Chernev, G. Berggren, et al., Room-temperature energy-sampling Kβ X-ray emission spectroscopy of the Mn4Ca complex of photosynthesis reveals three manganese-centered oxidation steps and suggests a coordination change prior to O2 formation, Biochemistry 55 (30) (2016) 4197–4211.

[6] S.C. Jensen, K.M. Davis, B. Sullivan, et al., X-ray emission spectroscopy of biomimetic Mn coordination complexes, J. Phys. Chem. Lett. 8 (12) (2017) 2584–2589.

[7] H.W. Liang, Th. Kroll, D. Nordlund, T.-C. Weng, et al., Charge and spin-state characterization of cobalt bis(o-dioxolene) valence tautomers using Co Kβ X-ray emission and L-edge X-ray absorption spectroscopies, Inorg. Chem. 56 (2) (2017) 737–747.

[8] S. Lafuerza, J. García, G. Subías, et al., High-resolution Mn K-edge x-ray emission and absorption spectroscopy study of the electronic and local structure of the three different phases in Nd0.5Sr0.5MnO3, Phys. Rev. B 93 (2016) 205108.

[9] S. Lafuerza, A. Carlantuono, M. Retegan, et al., Chemical sensitivity of Kβ and Kα X-ray emission from a systematic investigation of iron compounds, Inorg. Chem. 59 (17) (2020) 12518–12535.

[10] G. Vankó, Th. Neisius, G. Molnár, et al., Transitions, probing the 3d spin momentum with X-ray emission spectroscopy: The case of molecular-spin, J. Phys. Chem. B 110 (24) (2006) 11647–11653.

[11] G. Vankó, P. Glatzel, V.-T. Pham, et al., Picosecond time-resolved X-ray emission spectroscopy: Ultrafast spin-state determination in an iron complex, Angew. Chem. Int. Edn 49 (2010) 5910–5912.

[12] W. Zhang, R. Alonso-Mori, U. Bergmann, et al., Tracking excited-state charge and spin dynamics in iron coordination complexes, Nature 509 (2014) 345–348.

[13] S. Canton, C. Kjær, G. Vankó, et al., Visualizing the non-equilibrium dynamics of photoinduced intramolecular electron transfer with femtosecond X-ray pulses, Nature Commun. 6 (2015) 6359.

[14] G. Vankó, A. Bordage, et al., Spin-state studies with XES and RIXS: From static to ultrafast, J. Electron Spectrosc. Relat. Phenom. 188 (2013) 166–171.

[15] K.S. Kjær, et al., Ligand manipulation of charge transfer excited state relaxation and spin crossover in [Fe(2, 2′-bipyridine)2(CN)2], Struct. Dyn. 4 (2017) 044030.

[16] W. Zhang, K.S. Kjær, et al., Manipulating charge transfer excited state relaxation and spin crossover in iron coordination complexes with ligand substitution, Chem. Sci. 8 (2017) 515–523.

[17] K. Kunnus, M. Vacher, T.C.B. Harlang, et al., Vibrational wavepacket dynamics in Fe carbene photosensitizer determined with femtosecond X-ray emission and scattering, Nature Commun. 11 (2020) 634.

[18] M. Ibrahim, et al., Untangling the sequence of events during the S2→ S3transition in photosystem II and implications for thewater oxidation mechanism, Proc. Natl. Acad. Sci. USA 117 (23) (2020) 12624–12635.

[19] D. Kinschel, C. Bacellar, O. Cannelli, et al., Femtosecond X-ray emission study of the spin cross-over dynamics in haem proteins, Nature Commun. 11 (2020) 4145.

[20] C. Bacellar, et al., Spin cascade and doming in ferric hemes: FemtosecondX-ray absorption and X-ray emission studies, Proc. Natl. Acad. Sci. USA 117 (36) (2020) 21914–21920.

[21] M.A. Naumova, A. Kalinko, et al., Revealing hot and long-lived metastable spin states in the photoinduced switching of solvated metallogrid complexes with femtosecond optical and X-ray spectroscopies, J. Phys. Chem. Lett. 11 (6) (2020) 2133–2141.

[22] W. Decking, S. Abeghyan, P. Abramian, et al., A MHz-repetition-rate hard X-ray free-electron laser driven by a superconducting linear accelerator, Nat. Photonics 14 (2020) 391–397.

[23] A.M. March, et al., Feasibility of valence-to-core X-ray emission spectroscopy for tracking transient species, J. Phys. Chem. C 119 (26) (2015) 14571–14578.

[24] A.M. March, et al., Probing transient valence orbital changes with picosecond valence-to-core X-ray emission spectroscopy, J. Phys. Chem. C 121 (5) (2017) 2620–2626.

[25] K. Ledbetter, et al., Excited state charge distribution and bond expansion of ferrous complexes observed with femtosecond valence-to-core x-ray emission spectroscopy, J. Chem. Phys. 152 (2020) 074203.

[26] A. Galler, et al., Scientific instrument femtosecond X-ray experiments (FXE): instrumentation and baseline experimental capabilities, J. Synchrotron Radiat. 26 (2019) 1432–1447.

[27] D. Khakhulin, et al., Ultrafast X-ray photochemistry at European XFEL: Capabilities of the femtosecond X-ray experiments (FXE) instrument, Appl. Sci. 10 (3) (2020) 995.

[28] R. Alonso-Mori, et al., A multi-crystal wavelength dispersive x-ray spectrometer, Rev. Sci. Instrum. 83 (2012) 073114.

[29] J. Szlachetko, et al., A von Hamos x-ray spectrometer based on a segmented-type diffraction crystal for single-shot x-ray emission spectroscopy and time-resolved resonant inelastic x-ray scattering studies, Rev. Sci. Instrum. 83 (2012) 103105.

[30] R. Alonso-Mori, et al., Energy-dispersive X-ray emission spectroscopy using an X-ray free-electron laser in a shot-by-shot mode, Proc. Natl. Acad. Sci. USA 109 (47) (2012) 19103–19107.

[31] A. Kalinko, et al., A von Hamos-type hard X-ray spectrometer at the PETRA III beamline P64, J. Synchrotron Radiat. 27 (2020) 31–36.

[32] T. Sato, Femtosecond timing synchronization at megahertz repetition rates for an x-ray free-electron laser, Optica 7 (6) (2020) 716–717.

[33] T.W. Guest, et al., Shot-to-shot two-dimensional photon intensity diagnostics within megahertz pulse-trains at the European XFEL, J. Synchrotron Radiat. 29 (2022) 939–946.

[34] J.H. Jungmann-Smith, et al., JUNGFRAU 0.2: prototype characterization of a gain-switching, high dynamic range imaging system for photon science at swissfel and synchrotrons, J. Instrum. 9 (2014) P12013.

[35] J.H. Jungmann-Smith, et al., Towards hybrid pixel detectors for energy-dispersive or soft X-ray photon science, J. Synchrotron Radiat. 23 (2016) 385–394.

[36] T.B. van Driel, et al., The epix10k 2-megapixel hard X-ray detector at LCLS, J. Synchrotron Radiat. 27 (2020) 608–615.

[37] R.M. Wheater, et al., Development of data correction for the 1M large pixel detector at the euxfel, J. Instrum. 17 (2022) P04013.

[38] Data recorded for the experiment at the European XFEL are available online, [Online], Available: http://dx.doi.org/10.22003/XFEL.EU-DATA-002708-00.

[39] G. Palmer, et al., Pump–probe laser system at the FXE and SPB/SFX instruments of the European X-ray Free-Electron Laser Facility, J. Synchrotron Radiat. 26 (2019) 328–332.

[40] S.E. Canton, et al., Ultrafast Jahn-Teller Photoswitching in Cobalt Single-Ion Magnets, Adv. Sci. (2023) 2206880.

[41] C. Stan, D. Milathianaki, H. Laksmono, et al., Liquid explosions induced by X-ray laser pulses, Nature Phys. 12 (2016) 966–971.

[42] P. Vagovič, et al., Megahertz x-ray microscopy at x-ray free-electron laser and synchrotron sources, Optica 6 (9) (2019) 1106–1109.

[43] H.N. Chapman, C. Caleman, N. Timneanu, Diffraction beforedestruction, Philos. Trans. R. Soc. B 369 (2014) 20130313.

[44] W. Błachucki, Y. Kayser, J. Czapla-Masztafiak, et al., Inception of electronic damage of matter by photon-driven post-ionization mechanisms, Struct. Dyn. 6 (2019) 024901.

[45] R. Alonso-Mori, D. Sokaras, M. Cammarata, et al., Femtosecond electronic structure response to high intensity XFEL pulses probed by iron X-ray emission spectroscopy, Sci. Rep. 10 (2020) 16837.

[46] M. Vakili, et al., 3D printed devices and infrastructure for liquid sample delivery at the European XFEL, J. Synchrotron Radiat. 29 (2022) 331–346.

[47] S. Redford, et al., First full dynamic range calibration of the JUNGFRAU photon detector, J. Instrum. 13 (2018) C01027.

[48] S. Redford, et al., First full dynamic range scan of the JUNGFRAU detector performed at an XFEL with an accurate intensity reference, J. Instrum. 15 (2020) C02025.

[49] A. Mozzanica, et al., The GOTTHARD charge integrating readout detector: design and characterization, J. Instrum. 7 (2012) C01019.

[50] J. Zhang, et al., Towards gotthard-II: development of a silicon microstrip detector for the European X-ray free-electron laser, J. Instrum. 13 (2018) P01025.

[51] G. Lutz, et al., DEPFET sensor with intrinsic signal compression developed for use at the XFEL free electron laser radiation source, Nucl. Instrum. Methods A 624 (2) (2010) 528–532.

[52] M. Porro, et al., The MiniSDD-based 1-Mpixel Camera of the DSSC project for the European XFEL, IEEE Trans. Nucl. Sci. 68 (2021) 1334–1350.

[53] D. Greiffenberg, et al., Optimization of the noise performance of the AGIPD prototype chips, J. Instrum. 8 (2013) P10022.

[54] A. Allahgholi, et al., Megapixels @ Megahertz – The AGIPD high-speed cameras for the European XFEL, Nucl. Instrum. Methods A 942 (2019) 162324.

[55] A. Allahgholi, et al., The adaptive gain integrating pixel detector at the European XFEL, J. Synchrotron Radiat. 26 (2019) 74–82.

[56] A. Koch, et al., Performance of an LPD prototype detector at MHz frame rates under synchrotron and FEL radiation, J. Instrum. 8 (2013) C11001.

[57] M. Hart, et al., Development of the LPD, a high dynamic range pixel detector for the European XFEL, in: Nuclear Science Symposium and Medical Imaging Conference Record, NSS/MIC, 2012, pp. 534–537.

[58] M.C. Veale, et al., Characterisation of the high dynamic range Large Pixel Detector (LPD) and its use at X-ray free electron laser sources, J. Instrum. 12 (2017) P12003.

[59] J. Zhang, et al., Design and first tests of the Gotthard-II readout ASIC for the European X-ray Free-Electron Laser, J. Instrum. 16 (2021) P04015.